

ARTICLES

Intrinsic motions along an enzymatic reaction trajectory

Katherine A. Henzler-Wildman¹, Vu Thai¹, Ming Lei¹, Maria Ott³, Magnus Wolf-Watz¹†, Tim Fenn²‡, Ed Pozharski²‡, Mark A. Wilson²‡, Gregory A. Petsko², Martin Karplus^{4,5}, Christian G. Hübner³† & Dorothee Kern¹

The mechanisms by which enzymes achieve extraordinary rate acceleration and specificity have long been of key interest in biochemistry. It is generally recognized that substrate binding coupled to conformational changes of the substrate–enzyme complex aligns the reactive groups in an optimal environment for efficient chemistry. Although chemical mechanisms have been elucidated for many enzymes, the question of how enzymes achieve the catalytically competent state has only recently become approachable by experiment and computation. Here we show crystallographic evidence for conformational substates along the trajectory towards the catalytically competent ‘closed’ state in the ligand-free form of the enzyme adenylate kinase. Molecular dynamics simulations indicate that these partially closed conformations are sampled in nanoseconds, whereas nuclear magnetic resonance and single-molecule fluorescence resonance energy transfer reveal rare sampling of a fully closed conformation occurring on the microsecond-to-millisecond timescale. Thus, the larger-scale motions in substrate-free adenylate kinase are not random, but preferentially follow the pathways that create the configuration capable of proficient chemistry. Such preferred directionality, encoded in the fold, may contribute to catalysis in many enzymes.

A folded protein is not a unique structure, but includes an ensemble of folded substates that are sampled at physiological temperatures^{1–4}. As pointed out about 40 years ago⁵, protein folding cannot proceed by random sampling of all possible conformations. In analogy to the energy landscape view of the folding process^{6,7}, rearrangements within a folded protein are similarly directed by the energy landscape^{1,4}. Although the lowest energy structures can often be determined experimentally, an understanding of other conformations and the transitions among them is still in its infancy.

Synergy between structure and plasticity results in the unique power of biocatalysts (enzymes). The chemical mechanisms of many enzymatic reactions are known in great detail thanks to advances in classical enzymology and structural biology. For a number of enzymes, snapshots of conformations that are sampled during catalysis have been obtained using ligands, substrates and inhibitors. Recently, transitions between these states have been measured by nuclear magnetic resonance (NMR) relaxation experiments with substrate analogues^{8–11} or during catalysis^{12,13}, as well as by single-molecule fluorescence resonance energy transfer (FRET)^{14–19}. Here we explore how an enzyme, adenylate kinase, reaches a catalytically competent conformation in which the reactive groups are brought into close proximity in a position favouring catalysis. Using X-ray crystallography, NMR, single-molecule FRET, normal mode analysis (NMA) and molecular dynamics simulations, we identify conformational substates along this reaction trajectory that are already present in the substrate-free enzyme, and determine timescales for the transitions among them.

Open and closed conformation of *Aquifex* adenylate kinase

The crystal structure of adenylate kinase (Adk) from the hyperthermophile *Aquifex aeolicus* (*Aquifex* Adk) has been solved (Fig. 1). Adks are enzymes that maintain the cellular equilibrium concentration of

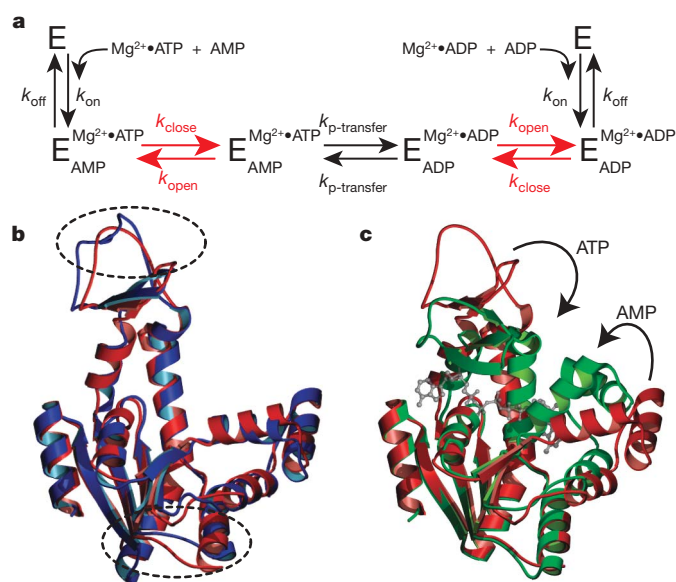


Figure 1 | Kinetic model and X-ray structure of *Aquifex* Adk. **a**, Proposed reaction scheme for the enzyme adenylate kinase (E) including the steps of substrate binding (k_{on}), lid closing (k_{close}), phospho-transfer ($k_{\text{p-transfer}}$), lid opening (k_{open}) and substrate dissociation (k_{off}). **b**, Superposition of molecule A (for definition, see Fig. 2) of apo *Aquifex* (red) with apo *E. coli* (blue) Adk reveals only small changes in the overall structure between the homologues, as indicated by dashed ovals. **c**, Superposition of apo *Aquifex* Adk (red) and *Aquifex* Adk in complex (green) with the substrate analogue Zn²⁺•Ap5A (shown as ball and stick in grey) demonstrates the closure of the ATP and AMP lids on substrate binding.

¹Department of Biochemistry and Howard Hughes Medical Institute, ²Department of Biochemistry, Brandeis University, Waltham, Massachusetts 02454, USA. ³Institute of Physics, Martin Luther–University Halle–Wittenberg, D-06120 Halle, Germany. ⁴Department of Chemistry and Chemical Biology, Harvard University, Cambridge, Massachusetts 02138, USA. ⁵Laboratoire de Chimie Biophysique, ISIS, Université Louis Pasteur, F-67000 Strasbourg, France. †Present addresses: University of Umeå, Department of Chemistry, SE-90187 Umeå, Sweden (M.W.-W.); Departments of Molecular and Cellular Physiology and Howard Hughes Medical Institute, Stanford University, Stanford, California 94305, USA (T.F.); Department of Pharmaceutical Sciences, University of Maryland, Baltimore, Maryland 21201, USA (E.P.); Department of Biochemistry and the Redox Biology Center, University of Nebraska, Lincoln, Nebraska 68588, USA (M.A.W.); University at Lübeck, Institute of Physics, 23538 Lübeck, Germany (C.G.H.).

adenylate nucleotides by catalysing the reversible conversion of ATP and AMP into two ADP molecules (Fig. 1a). Adks are homologous in sequence and structure²⁰, and typically have a core domain plus ATP and AMP lids. The overall structure of *Aquifex* Adk is strikingly similar to that of *Escherichia coli* Adk²¹. The most obvious differences are shortening of loops in the ATP lid and at the base of the AMP lid, and the presence of five additional prolines in *Aquifex* Adk²².

To explore conformational rearrangements sampled during catalysis, we solved the structure of *Aquifex* Adk complexed with the bi-substrate analogue Zn²⁺•Ap5A (Fig. 1c). Ap5A consists of two adenosine nucleosides covalently linked through a pentaphosphate. It binds tightly to Adk, mimicking the ternary complex²³. For phosphotransfer, both lids must close to exclude bulk water from the active site and to bring the substrates into position for phosphotransfer. Consequently, large conformational changes are observed on binding of Ap5A to *Aquifex* Adk that are very similar to the changes observed in other Adks in complex with Mg²⁺•Ap5A²³ or other substrates or analogues²⁰. A large number of X-ray structures of nucleoside monophosphate kinases with and without ligands were used previously to create a movie of ligand-induced conformational changes²⁰.

Substates in apo Adk along the reaction trajectory

Although those results would fit nicely with the standard view of ligand-induced conformational change between single apo and ligand-bound states, the combined crystallographic, NMR, single-molecule and computational studies demand a fundamentally different picture. The asymmetric unit of apo *Aquifex* Adk consists of three molecules (A, B and C) with significantly different conformations (Fig. 2). Stabilization of these three particular substates seems to be caused by crystal contacts (see Supplementary Figs 1 and 2). Although this phenomenon is known for other crystal structures (for examples, see refs 24–27), different conformations are more frequently observed in crystals of molecules with and without bound ligands.

Are these substates relevant for catalysis? A least-squares superposition of the C α atoms of these three molecules with the Zn²⁺•Ap5A-bound ‘fully closed’ form shows that these lid substates lie along a trajectory between the fully open and fully closed conformations (Fig. 2a). The substates of ligand-free Adk arise from hinge-bending motions of the lids relative to the core; the conformations within each domain are very similar among the substates (Fig. 2). Further bending of the same hinges results in full closure on inhibitor binding. These hinges have unique physical properties²² and are located at very similar positions in *E. coli* Adk^{21,28,29}. Although the hinges are found mostly in loop regions, one hinge for the ATP lid is located in the middle of a long α helix (hinge 8), which actually breaks into two helices on closure. The crystallographic results show the directionality of the rearrangements, but do not determine the probability of attaining these structures or the rates of transitions among them in solution.

Motions along the reaction trajectory measured by NMR

Previously reported snapshots of a series of conformations of Adks with and without bound nucleotides have been shown to lie on a calculated path between the open and closed state^{20,29}. Moreover, the transition from the closed to the open state has been shown recently to limit the overall catalytic rate¹³.

To address the question of whether the conformational sampling seen in the crystal structure also occurs in solution, ¹⁵N NMR relaxation dispersion experiments were performed on apo *Aquifex* Adk (Fig. 3a, c). These experiments allow detection of residues that undergo changes in their local chemical environments and characterization of the kinetics¹⁰. In an NMR experiment, conformational exchange in the microsecond-to-millisecond timescale causes increased dephasing of coherence, resulting in additional line-broadening of NMR signals by an amount (R_{ex}) that contributes to the measured overall transverse

relaxation rate (R_2^{eff}). R_{ex} can be refocused by increasing the power of an applied radio-frequency field (ν_{CPMG} , where CPMG stands for Carr–Purcell–Meiboom–Gill). From the dependence of R_{ex} on ν_{CPMG} explored in the relaxation dispersion experiment (Fig. 3a), three physical parameters for a two-site dynamic process can, in principle, be obtained: rates of interconversion (k_{ex}), relative populations of the exchanging species (p_A and p_B) and chemical shifts between the exchanging species ($\Delta\omega$) (see Methods).

Residues located in the hinge regions and in parts of both lids that show conformational heterogeneity in the crystal also show chemical exchange in solution (Fig. 3c). In these areas, fluctuations among the crystallographic substates would cause changes in the local environment, and consequently detectable chemical exchange. In contrast, nuclei in regions where motion does not cause any changes in their electronic environment, such as within a rigid domain, will not display R_{ex} in this experiment. We stress that the measured R_{ex} , manifested in the amplitude of the dispersion profiles, is related directly to $\Delta\omega$. Spatial information cannot be inferred from these data, but the kinetics of the fluctuations can be measured.

To quantitatively compare the kinetics of lid movement in apo *Aquifex* Adk with the kinetics during turnover¹³, ¹⁵N relaxation experiments were performed under the same physical conditions at 20 °C. However, the rates were too fast in apo *Aquifex* Adk (rates of 2,000–7,000 s⁻¹ are compatible with the dispersion data, see Supplementary Fig. 6) for accurate analysis. Therefore, the experiments were repeated at 10 °C with perdeuterated protein. The lower temperature brings the rates into a time regime that is well determined

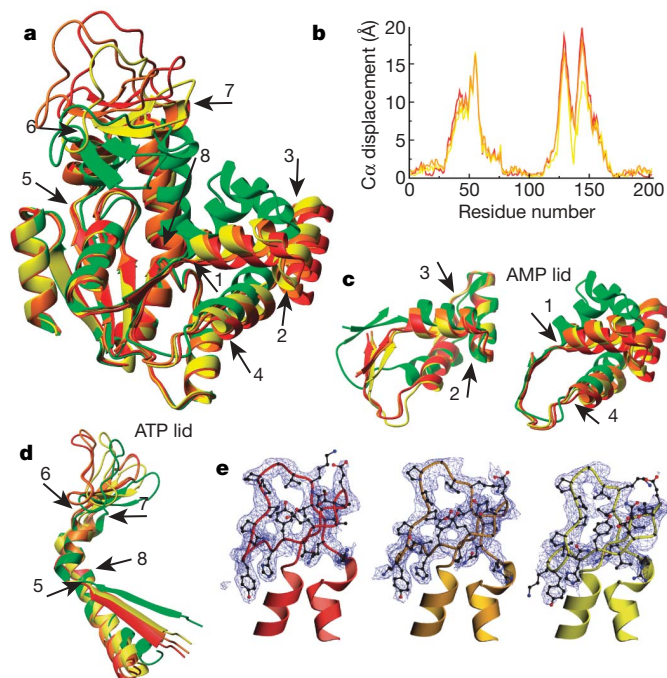


Figure 2 | Conformational substates of ligand-free *Aquifex* Adk detected in the crystal structure. **a**, Superposition of the three molecules, A, B and C, in the asymmetric unit of apo Adk (red, orange and yellow, respectively) and Adk complexed with Zn²⁺•Ap5A (green; Zn²⁺ from the crystallization mother liquor is bound to the Mg²⁺ site). The substates A, B and C lie along the reaction trajectory towards the closed state. **b**, Backbone displacement of A (red), B (orange) and C (yellow) relative to the inhibitor-bound form. **c**, **d**, The conformational substates A, B and C are a result of motions around eight hinges, indicated by arrows (for details about the hinges, see ref. 22). For better visualization of the hinges of the ATP lid, the latter was rotated by 90° (**d**) with respect to **a**. The two views in **c** show the AMP lid with different segments overlaid to highlight the two distinct hinge pairs. **e**, $2F_o - F_c$ maps contoured at 1.0σ of the ATP lids of molecules A (left), B (centre) and C (right) show the quality of the electron density.

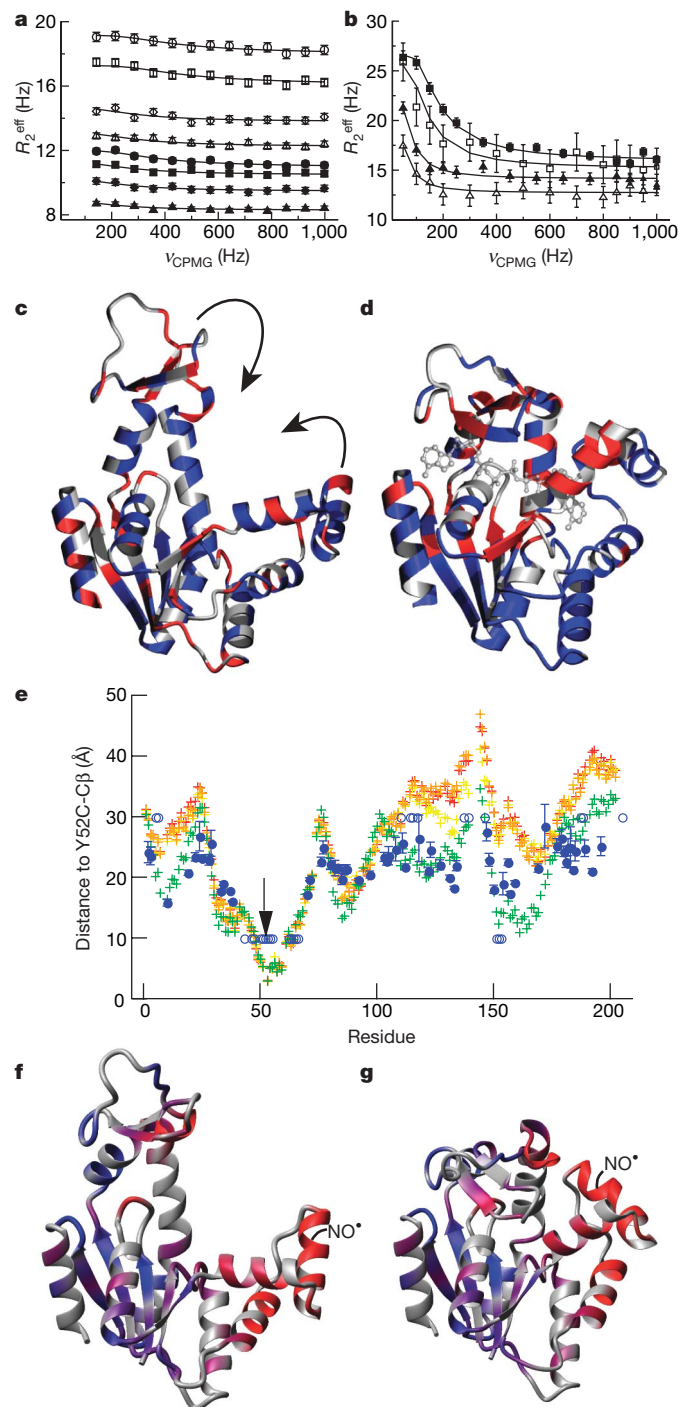


Figure 3 | Characterization of millisecond dynamics of *Aquifex Adk* in solution by NMR. **a–d**, The dependence of the ^{15}N effective transverse relaxation time (R_2^{eff}) on an applied radio-frequency field (ν_{CPMG})⁴⁶ for representative residues of $^2\text{H}/^{15}\text{N}$ apo Adk at 10 °C (**a**) and $^1\text{H}/^{15}\text{N}$ Adk in complex with $\text{Mg}^{2+}\cdot\text{Ap5A}$ at 20 °C (**b**) with errors bars (± 1 s. d.) based on duplicates and signal-to-noise ratios. Residues with conformational exchange (red), without exchange (blue) and overlapped or proline residues (grey) are mapped onto the crystal structure of apo Adk (**c**) and Adk complexed with $\text{Mg}^{2+}\cdot\text{Ap5A}$ (**d**). **e–g**, PRE by a spin label ($\text{NO}\cdot$) at residue 52 indicates that ligand-free Adk samples conformations resembling the closed state. **e**, Distances calculated from Y52C-C β to each amide proton for molecule A (red), B (orange) and C (gold) of apo Adk and inhibitor-bound Adk (green) are compared to distances calculated from the spin-label-induced line-broadening for ligand-free Adk (blue, error bars are ± 1 s. d.). Open circles represent H_N that are broadened beyond detection owing to the close proximity to the spin label (shown at 10 Å) or have no observable line broadening (shown at 30 Å). The PRE-derived distances are plotted onto the structure of the open (**f**) and closed (**g**) conformation as a continuous colour scale from blue (far away) to red (close proximity).

by CPMG relaxation experiments, whereas deuteration decreases the rate of transverse relaxation, resulting in a larger contribution of conformational exchange relative to the overall relaxation rate. Under these conditions, most of the exchanging residues can be fit with a single exchange rate of $950 \pm 150 \text{ s}^{-1}$ (mean \pm standard deviation (s.d.)) (Fig. 3a). Although this rate is well determined, the small amplitude of the dispersion profiles hampered characterization of the nature of the conformational transition.

The combination of crystallographic and NMR data indicate that the apo enzyme consists of an ensemble of conformations along the lid-motion trajectory required for catalytic function. Is a similar physical picture applicable for the inhibitor-bound, closed state? The X-ray structure shows one conformation (Fig. 1c). In contrast, ^{15}N relaxation dispersion experiments on $\text{Mg}^{2+}\cdot\text{Ap5A}$ -bound *Aquifex Adk* at 20 °C reveal conformational fluctuations with a rate of $300 \pm 150 \text{ s}^{-1}$ (mean \pm s.d.) that can be rationalized by a full opening/closing transition (Fig. 3b, d). Larger $\Delta\omega$ values in the presence of the ligand result in larger R_{ex} values, allowing a detailed analysis similar to the analysis during catalysis¹³. First, $\Delta\omega$ values calculated from the dynamics experiments are in agreement with the chemical shift differences between open and closed conformations (Supplementary Table 4 and Supplementary Fig. 4). Second, the calculated relative populations are highly skewed towards the closed state ($95 \pm 2\%$). These results imply that the enzyme fluctuates between the closed and open conformation, even in the presence of the inhibitor $\text{Mg}^{2+}\cdot\text{Ap5A}$, with the equilibrium shifted far towards the closed form. It is not surprising that the rates measured for Adk bound to $\text{Mg}^{2+}\cdot\text{Ap5A}$ differ from those measured in the presence of natural substrates ($\sim 1,600 \text{ s}^{-1}$)¹³ because in Ap5A both nucleotides are covalently connected, significantly altering the energy landscape.

Motions along the reaction trajectory by molecular dynamics

The experiments described above show that ligand-free Adk can exist in multiple conformations with variable degrees of closure, and that transitions occur in solution on a millisecond timescale. Computational methods provide a means to link these spatial and dynamic characteristics. First, we performed molecular dynamics simulations in explicit water (individual water molecules included in the simulation) starting from the three crystallographic substates of apo *Aquifex Adk*: A, B and C. The largest root-mean-square fluctuations are located in the lid regions, with similar motional amplitudes for all three substates (Fig. 4a). Essentially the same conformational space is sampled in 10 ns starting from any of the three conformations (Fig. 4c and Supplementary Fig. 9). Because a 10 ns simulation is long enough for one molecule to visit all three crystallographic conformations, the energy barriers for interconversion among these substates must be low. Furthermore, these simulations allow investigation of the correlations between the motions of the two lids, which cannot be measured in an ensemble-averaged experiment. From the time traces (Fig. 4b) and a covariance matrix calculated after superimposing the core domain of all snapshots (Supplementary Fig. 8), it is apparent that the two lids move independently, at least for the subspace sampled by the apo structure in 10 ns.

To address the question of whether the lid fluctuations are random or have preferred directionality, we performed a principal component analysis (PCA)³⁰ and a NMA³¹. Both methods calculate the directionality and frequency of motions. The lowest frequency modes are often correlated with experimentally observed conformational changes^{29,32,33}. For *Aquifex Adk*, comparison of the vector connecting the most open (apo molecule A) and closed (inhibitor-bound) structures with the calculated lowest frequency modes shows that the first and second modes of the PCA contribute 49% and 63%, respectively, to the functionally important transition between the open and the closed states; this is consistent with results from a PCA of *E. coli Adk*³⁴. NMA provides similar results, with 80% contribution of its

first mode to the experimentally observed direction of lid closure (Fig. 4d, e and Supplementary Fig. 10).

Notably, the three 'open substates', A, B and C, are virtually along the same conformational coordinate, consistent with hinge-bending accounting for the observed conformational transitions. Most of these hinges have been suggested to be responsible for lid closure on the basis of structural comparison of the open and closed conformations of a variety of mesophilic adenylate kinases^{21,28}. Recent computational pathway analysis of ligand-free *E. coli* Adk has also identified changes in these regions along the pathway^{29,33}. Importantly, our crystal structures provide experimental evidence for bending at all hinges in ligand-free *Aquifex* Adk. Moreover, we show that lid displacements observed in the crystal of apo Adk are not separated by large free energy barriers, whereas there is a significantly larger barrier to reach the fully closed state (NMR and single-molecule FRET experiments). These results are in agreement with the main barrier being closer to the closed conformation, as indicated by the pathway analysis^{29,33}.

Sampling of conformational substates by single-molecule FRET

Whereas the conformational substates seen in the X-ray structure of apo Adk were sampled in 10-ns molecular dynamics simulations, the NMR relaxation experiments were indicative of lid motions in the

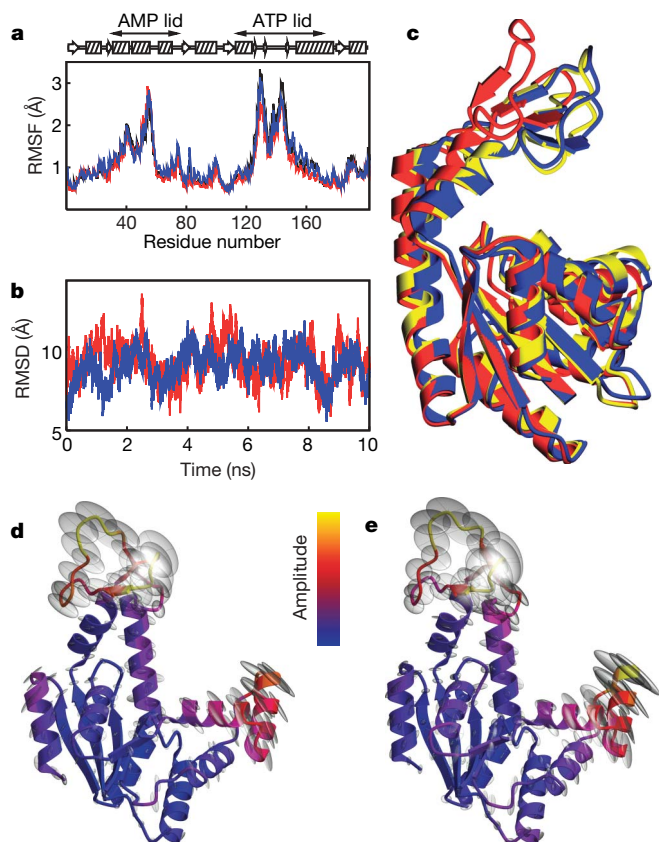


Figure 4 | Dynamics of *Aquifex* Adk computed by molecular dynamics simulations and normal mode analysis. **a**, The root mean square fluctuations (RMSF) are shown from 10-ns molecular dynamics simulations of molecule A (blue), B (red) and C (black) in explicit water. **b**, The corresponding time traces of the ATP lid (red) and AMP lid (blue) are visualized as root mean square deviation (RMSD) between simulated snapshots (starting from molecule A) and the crystal structure of the closed state. **c**, One snapshot (blue) from the molecular dynamics trajectory of molecule A is superimposed onto the crystal structures of molecule A (red) and molecule C (yellow). Relative amplitudes and directions of the ten combined lowest frequency modes calculated by PCA³⁰ (**d**) and NMA³¹ (**e**) are visualized by the direction and size of the silver ellipsoids together with the colour scale.

millisecond time regime. However, the NMR data did not provide information about the amplitude of motion. To address this difference in timescale between molecular dynamics simulations and NMR, we performed single-molecule FRET experiments³⁵. *Aquifex* Adk was fluorescently labelled using Alexa488 as the donor and Alexa633 as the acceptor in the AMP and ATP lids. The dyes (calculated Förster radius, R_0 , of 48 Å) and labelling sites were selected to optimally detect lid–lid distance changes going from the most open to the fully closed state (Fig. 5a). The enzymatic activity of the labelled enzyme is 35% of that of the wild type³⁶.

First we measured single-molecule FRET efficiency (E_t) distributions of both the ligand-free and the Mg^{2+} •Ap5A-bound form diffusing freely in solution (Fig. 5b, c)³⁷. FRET efficiencies were calculated from the total photon counts emitted by the donor and acceptor during the dwell time in the focus of the laser. The Mg^{2+} •Ap5A-bound form was used as a reference point for calibration of relative FRET efficiencies with respect to distance¹⁸. On the basis of our NMR data, the Mg^{2+} •Ap5A-bound form is highly skewed towards the fully closed conformation (Fig. 3b, d). This result is clearly reinforced by single-molecule FRET, which has the major population centred at $E_t = 0.83$ (corresponding to the closed state) with a tail at lower E_t values (open states) (Fig. 5c).

Interestingly, a similar closed state is sampled to a significant fraction even in the absence of any ligand (Fig. 5b). However, most of the ligand-free molecules have lower FRET efficiencies corresponding to conformations with increased lid–lid distances. The width of the distributions is caused by shot noise (see Methods), and the peak values correspond to lid–lid distances of the fully open and closed conformations. Two key conclusions can be drawn. First, apo Adk seems to sample both open and closed states in solution. Second, the timescale of interconversion between the open and closed conformations must be on the order of the residence time of the molecules in the focus (about 0.1 ms, as determined by fluorescence correlation spectroscopy, data not shown) or slower, because complete averaging of the FRET efficiencies would occur for much faster internal motions, resulting in a single E_t distribution³⁸.

To quantify the rates of lid opening and closing, transient fluorescence intensities of both the donor and the acceptor were recorded for individual Adk molecules immobilized on the surface of the microscope coverslip (Fig. 5d). The immobilized Adk molecules have full catalytic activity as probed by a luciferase assay (Supplementary Fig. 13). Indeed, opening and closing events could be detected directly for ligand-free Adk using 200- μ s bin times. The similarity of the shape of the E_t histogram from the time traces (Fig. 5d) and the diffusion experiment (Fig. 5b) is a nice demonstration of ergodicity of the system. Instead of setting a unique threshold value for discriminating closed and open states, an 'ambiguous zone' was defined for E_t values where the distributions of the open and closed states overlap (Fig. 5b–d). A change of state was assigned only when the ambiguous zone was crossed by E_t values. The lifetime distributions of open and closed states followed exponential statistics (Fig. 5e, f). Because the fitted rates were similar to the experimental time resolution it was apparent that those raw rates had to be corrected for missed events (see Methods), yielding opening and closing rates of $6,500 \pm 500 \text{ s}^{-1}$ and $2,000 \pm 200 \text{ s}^{-1}$ (mean \pm s.d.), respectively.

Clear evidence for our interpretation of opening/closing comes from a correlation analysis exhibiting pronounced anti-correlation in the cross-correlation function (Fig. 5g, details in Methods). The overall rate of these fluctuations is $7,000 \pm 2,000 \text{ s}^{-1}$ (mean \pm s.d.), in very good agreement with the sum of opening and closing rates obtained from the E_t -state analysis above and from NMR experiments at 20 °C ($k_{\text{open}} + k_{\text{close}}$ between 2,000 and 7,000 s^{-1} , Supplementary Fig. 6). Similar time-resolved single-molecule FRET experiments were performed on Mg^{2+} •Ap5A-bound Adk, showing slower opening/closing transitions; this is in agreement with the kinetics measured by NMR (Fig. 3b and Supplementary Figs 16 and 17). It is important to note that we are using an oversimplified two-state model. In reality,

more states are sampled, such as single-lid-closed conformations²⁰. It is possible that these single-lid-closed conformations are responsible for the smaller ratio between the open and closed populations determined by the single-molecule FRET experiments relative to the more skewed populations estimated from NMR experiments. These questions will be addressed in future experiments using three-colour FRET on triple-labelled Adk.

Sampling of conformational substates by NMR PRE

To corroborate our finding that ligand-free Adk in solution samples a substate similar to the fully closed inhibitor-bound crystal structure, we measured paramagnetic NMR relaxation enhancement effects (PRE)³⁹ from a spin label attached to the AMP lid (Fig. 3e–g). An unpaired electron increases the relaxation rate of other nuclei in an r^{-6} distance-dependent manner³⁹. Notably, severe line broadening

was observed for residues in the ATP lid that are far away from the spin-label attachment point in the open substates, in addition to the expected large effect on residues that are close to the spin-label site. However, all residues with line-broadening effects are clustered within a 30 Å radius of the spin label when mapped on the fully closed conformation (Fig. 3g). In an ensemble of conformations, short distances will dominate the observed PRE effects owing to the r^{-6} -distance-dependence, thus biasing the distance distribution. Therefore, the close agreement of the calculated PRE distances with the ones from the closed state should not be misinterpreted as a high population of the closed state for ligand-free Adk. The PRE data do not provide rates for the conformational transitions or populations. However, they unambiguously demonstrate sampling of states structurally similar to the closed state because distances from the spin label to all amides within 30 Å are detected. This method is complementary to the FRET method, which directly measures rates and populations but only a single distance.

Discussion

For catalysis, defined conformational changes pre-organize active-site residues in the configuration needed to facilitate chemistry^{40–42}. Random sampling of all possible folded configurations would degrade catalytic efficiency, a situation analogous to protein folding, which is similarly biased so as to sample only a small portion of the energy landscape. This concept of a hierarchy of substates has been pioneered by extensive studies on myoglobin^{1,3,4}. Here we show that motions in apo Adk occur preferentially in the direction of the catalytically competent closed conformation. The NMR relaxation dispersion, single-molecule FRET and paramagnetic relaxation enhancement experiments reveal that in the absence of substrate, Adk samples a minor state that is comparable to the closed state observed during catalysis. The concept of preferred fluctuations to states resembling the substrate-bound states directed by the energy landscape has been discussed recently⁴³. Although the large amplitude conformational transition in Adk is a relatively slow (microsecond-to-millisecond), infrequent event, faster (nanosecond) and more frequent transitions of smaller amplitude along the same trajectory are revealed by combining X-ray crystallography, molecular dynamics simulations and normal mode calculations. This hierarchy in space and time indicates that slow conformational transitions occurring on the timescale of catalytic turnover are facilitated by individual high-frequency local fluctuations^{2,22,44}. Biological function is the property selected by evolution. Thus, optimization of the energy landscape by selection of the substates and pathways needed for function is an element of efficient catalysis at physiological temperatures.

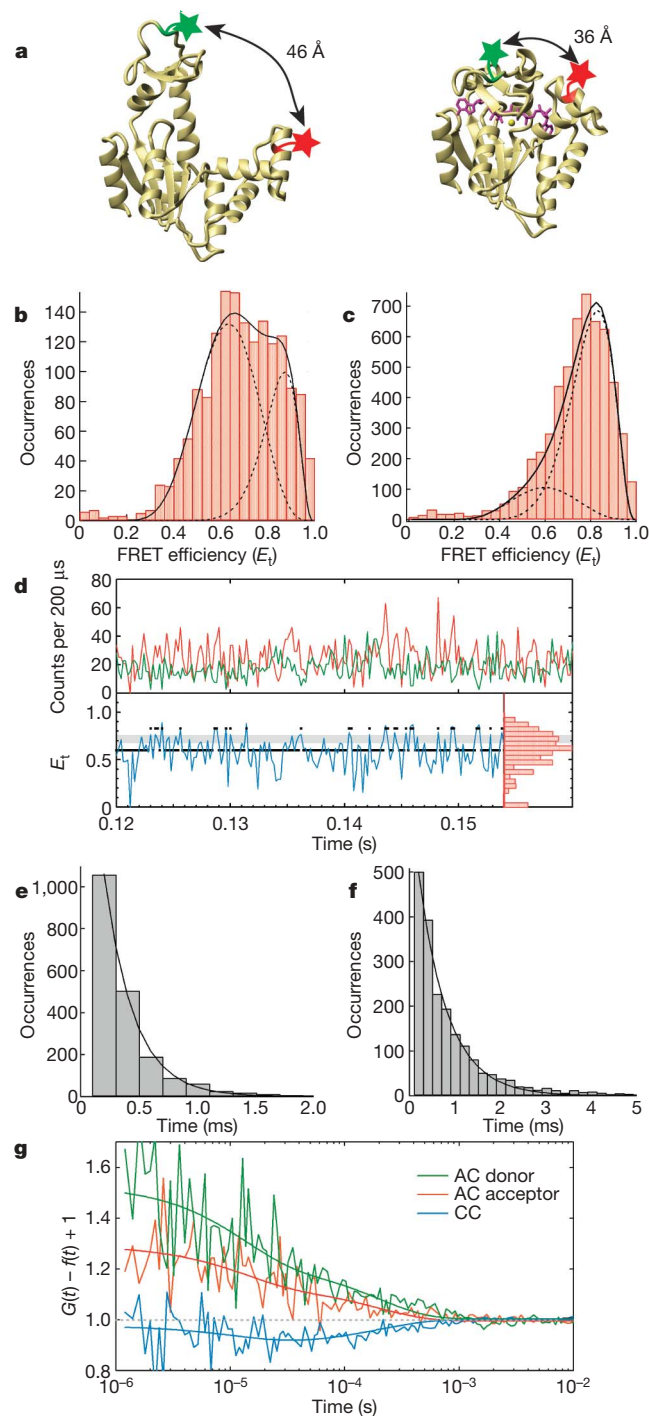


Figure 5 | Opening and closing of *Aquifex* Adk in solution by single-molecule FRET.

a, Positions of fluorescent dyes Alexa488 (green) and Alexa633 (red) on Adk at residue 52 (AMP lid, right) and 145 (ATP lid, top) or vice versa. **b, c**, Histograms of FRET efficiencies of ligand-free (**b**) and Mg^{2+} - \bullet Ap5A-bound (**c**) Adk measured from single-molecule diffusion experiments. The dashed lines represent gaussian fits of the corresponding distance histograms back-transformed into FRET efficiency (E_t), and the solid line is the sum of those distributions. **d**, Section of a single-molecule fluorescence time trace of ligand-free Adk tethered on a glass surface. Donor (green) and acceptor (red) intensities are shown together with the corresponding E_t (blue), including the E_t histogram over 25 time traces (red, right). Lifetimes of the open and closed state (black lines) were determined on the basis of a transition zone for E_t values, where the gaussian distributions of the open and closed states overlap (grey). **e, f**, The resulting lifetimes of 25 time traces were averaged, fitted exponentially and corrected for missed events and triplet-state dynamics to yield $k_{open} = 6,500 \pm 500 s^{-1}$ (**e**, mean \pm s.d.) and $k_{close} = 2,000 \pm 200 s^{-1}$ (**f**), respectively. **g**, The intensity correlation function, $G(t)$, for auto-correlation (AC) and cross-correlation (CC) analysis averaged over six immobilized ligand-free Adk molecules. Anti-correlation of the cross-correlation function is observed in the 10^{-4} to 10^{-3} s time region with a fitted overall opening/closing rate of $7,000 \pm 2,000 s^{-1}$ (mean \pm s.d.).

METHODS SUMMARY

Aquifex Adk was expressed and purified as described¹³. Fluorescently labelled Adk was prepared using Y52C and V145C mutants for labelling with Alexa633-maleimide and Alexa488-maleimide, and a 6×His tag on the carboxy terminus for tethering to a surface. Spin-labelled Adk was prepared using ¹⁵N-Adk(Y52C), which was reacted with (1-oxyl-2,2,5,5-tetramethyl-Δ3-pyrroline-3-methyl) methanethiosulfonate (MTSL) for 12 hours at 25 °C. Diffraction data of crystals of apo Adk and of Adk complexed with Zn²⁺•Ap5A were collected both at room temperature and at cryogenic temperature. Translation-libration-screw (TLS)⁴⁵ refinement was performed, dividing the three molecules into the core, the ATP lid and the AMP lid. Constant time ¹⁵N backbone CPMG relaxation dispersion experiments⁴⁶ were acquired in an interleaved manner incorporating transverse relaxation optimized spectroscopy (TROSY) selection⁴⁷ and fit as described¹². The effect of the spin label was determined by comparing the peak intensity in a pair of heteronuclear single quantum correlation (HSQC) spectra taken on the paramagnetic and diamagnetic form. The data were interpreted using ¹H R₂ values measured on the diamagnetic sample and converted to distances assuming a correlation time equal to the global tumbling time³⁹, measured for the unlabelled protein (τ_c)²². Molecular dynamics simulations were performed using the program CHARMM⁴⁸. Single-molecule FRET measurements were performed using a home-built sample-scanning optical confocal microscope. The transfer efficiency E_t for each burst was calculated according to the equation:

$$E_t = (I_A)/(I_A + I_D)$$

where I_D and I_A are the corrected intensity of the donor and acceptor channel, respectively, on donor excitation. Transient intensities on immobilized proteins were recorded with an acquisition time of 100 ns. The intensity time trace of a tethered molecule was taken by integrating photon counts for donor and acceptor channels with bin times between 200 μs and 1 ms. Auto- and cross-correlation functions were calculated from unbinned data for each individual molecule, subsequently averaged and globally fit.

Full Methods and any associated references are available in the online version of the paper at www.nature.com/nature.

Received 14 April; accepted 26 October 2007.

Published online 18 November 2007.

- Austin, R. H., Beeson, K. W., Eisenstein, L., Frauenfelder, H. & Gunsalus, I. C. Dynamics of ligand binding to myoglobin. *Biochemistry* **14**, 5355–5373 (1975).
- McCammon, J. A., Gelin, B. R. & Karplus, M. Dynamics of folded proteins. *Nature* **267**, 585–590 (1977).
- Frauenfelder, H., Sligar, S. G. & Wolynes, P. G. The energy landscapes and motions of proteins. *Science* **254**, 1598–1603 (1991).
- Frauenfelder, H., McMahon, B. H. & Fenimore, P. W. Myoglobin: the hydrogen atom of biology and a paradigm of complexity. *Proc. Natl Acad. Sci. USA* **100**, 8615–8617 (2003).
- Levinthal, C. Are there pathways for protein folding. *J. Chim. Phys. Phys.-Chim. Biol.* **65**, 44–45 (1968).
- Bryngelson, J. D., Onuchic, J. N., Socci, N. D. & Wolynes, P. G. Funnels, pathways, and the energy landscape of protein folding: a synthesis. *Proteins* **21**, 167–195 (1995).
- Dobson, C. M., Sali, A. & Karplus, M. Protein folding: a perspective from theory and experiment. *Angew. Chem. Int. Ed.* **37**, 868–893 (1998).
- Williams, J. C. & McDermott, A. E. Dynamics of the flexible loop of triosephosphate isomerase: the loop motion is not ligand gated. *Biochemistry* **34**, 8309–8319 (1995).
- Boehr, D. D., McElheny, D., Dyson, H. J. & Wright, P. E. The dynamic energy landscape of dihydrofolate reductase catalysis. *Science* **313**, 1638–1642 (2006).
- Palmer, A. G. NMR characterization of the dynamics of biomacromolecules. *Chem. Rev.* **104**, 3623–3640 (2004).
- Cui, Q. & Karplus, M. Catalysis and specificity in enzymes: a study of triosephosphate isomerase and comparison with methyl glyoxal synthase. *Adv. Protein Chem.* **66**, 315–372 (2003).
- Eisenmesser, E. Z. *et al.* Intrinsic dynamics of an enzyme underlies catalysis. *Nature* **438**, 117–121 (2005).
- Wolf-Watz, M. *et al.* Linkage between dynamics and catalysis in a thermophilic-mesophilic enzyme pair. *Nature Struct. Mol. Biol.* **11**, 945–949 (2004).
- Blanchard, S. C., Gonzalez, R. L., Kim, H. D., Chu, S. & Puglisi, J. D. tRNA selection and kinetic proofreading in translation. *Nature Struct. Mol. Biol.* **11**, 1008–1014 (2004).
- Ha, T. *et al.* Single-molecule fluorescence spectroscopy of enzyme conformational dynamics and cleavage mechanism. *Proc. Natl Acad. Sci. USA* **96**, 893–898 (1999).
- Myong, S., Stevens, B. C. & Ha, T. Bridging conformational dynamics and function using single-molecule spectroscopy. *Structure* **14**, 633–643 (2006).
- Rothwell, P. J. *et al.* Multiparameter single-molecule fluorescence spectroscopy reveals heterogeneity of HIV-1 reverse transcriptase: primer/template complexes. *Proc. Natl Acad. Sci. USA* **100**, 1655–1660 (2003).
- Schuler, B., Lipman, E. A. & Eaton, W. A. Probing the free-energy surface for protein folding with single-molecule fluorescence spectroscopy. *Nature* **419**, 743–747 (2002).
- Zhang, Z., Rajagopalan, P. T. R., Selzer, T., Benkovic, S. J. & Hammes, G. G. Single-molecule and transient kinetics investigation of the interaction of dihydrofolate reductase with NADPH and dihydrofolate. *Proc. Natl Acad. Sci. USA* **101**, 2764–2769 (2004).
- Vonrhein, C., Schlauderer, G. J. & Schulz, G. E. Movie of the structural changes during a catalytic cycle of nucleoside monophosphate kinases. *Structure* **3**, 483–490 (1995).
- Müller, C. W., Schlauderer, G. J., Reinstein, J. & Schulz, G. E. Adenylate kinase motions during catalysis: an energetic counterweight balancing substrate binding. *Structure* **4**, 147–156 (1996).
- Henzler-Wildman, K. A. *et al.* A hierarchy of timescales in protein dynamics is linked to enzyme catalysis. *Nature* doi:10.1038/nature06407 (this issue).
- Müller, C. W. & Schulz, G. E. Structure of the complex between adenylate kinase from *Escherichia coli* and the inhibitor Ap5A refined at 1.9 Å resolution. A model for a catalytic transition state. *J. Mol. Biol.* **224**, 159–177 (1992).
- Błaszczak, J., Li, Y., Yan, H. G. & Ji, X. H. Crystal structure of unligated guanylate kinase from yeast reveals GMP-induced conformational changes. *J. Mol. Biol.* **307**, 247–257 (2001).
- Faber, H. R. & Matthews, B. W. A mutant T4 lysozyme displays 5 different crystal conformations. *Nature* **348**, 263–266 (1990).
- Gardberg, A., Shuvalova, L., Monnerjahn, C., Konrad, M. & Lavie, A. Structural basis for the dual thymidine and thymidylate kinase activity of herpes thymidine kinases. *Structure* **11**, 1265–1277 (2003).
- Odintsov, S. G., Sabala, I., Bourenkov, G., Rybin, V. & Bochtler, M. Substrate access to the active sites in aminopeptidase T, a representative of a new metallopeptidase clan. *J. Mol. Biol.* **354**, 403–412 (2005).
- Gerstein, M., Schulz, G. & Chothia, C. Domain closure in adenylate kinase — joints on either side of 2 helices close like neighboring fingers. *J. Mol. Biol.* **229**, 494–501 (1993).
- Maragakis, P. & Karplus, M. Large amplitude conformational change in proteins explored with a plastic network model: adenylate kinase. *J. Mol. Biol.* **352**, 807–822 (2005).
- Karplus, M. & Kushick, J. N. Method for estimating the configurational entropy of macromolecules. *Macromolecules* **14**, 325–332 (1981).
- Ma, J. & Karplus, M. Ligand-induced conformational changes in ras p21: a normal mode and energy minimization analysis. *J. Mol. Biol.* **274**, 114–131 (1997).
- Bahar, I. & Rader, A. J. Coarse-grained normal mode analysis in structural biology. *Curr. Opin. Struct. Biol.* **15**, 586–592 (2005).
- Miyashita, O., Onuchic, J. N. & Wolynes, P. G. Nonlinear elasticity, proteinquakes, and the energy landscapes of functional transitions in proteins. *Proc. Natl Acad. Sci. USA* **100**, 12570–12575 (2003).
- Lou, H. & Cukier, R. I. Molecular dynamics of apo-adenylate kinase: a principal component analysis. *J. Phys. Chem. B* **110**, 12796–12808 (2006).
- Ha, T. *et al.* Probing the interaction between two single molecules: fluorescence resonance energy transfer between a single donor and a single acceptor. *Proc. Natl Acad. Sci. USA* **93**, 6264–6268 (1996).
- Rhoads, D. G. & Lowenstein, J. M. Initial velocity and equilibrium kinetics of myokinase. *J. Biol. Chem.* **243**, 3963–3972 (1968).
- Nie, S., Chiu, D. T. & Zare, R. N. Probing individual molecules with confocal fluorescence microscopy. *Science* **266**, 1018–1021 (1994).
- Margittai, M. *et al.* Single-molecule fluorescence resonance energy transfer reveals a dynamic equilibrium between closed and open conformations of syntaxin 1. *Proc. Natl Acad. Sci. USA* **100**, 15516–15521 (2003).
- Iwahara, J., Tang, C. & Clore, G. M. Practical aspects of ¹H transverse paramagnetic relaxation enhancement measurements on macromolecules. *J. Magn. Reson.* **184**, 185–195 (2007).
- Bruice, T. C. Computational approaches: reaction trajectories, structures, and atomic motions. Enzyme reactions and proficiency. *Chem. Rev.* **106**, 3119–3139 (2006).
- Hammes-Schiffer, S. & Benkovic, S. J. Relating protein motion to catalysis. *Annu. Rev. Biochem.* **75**, 519–541 (2006).
- Nagel, Z. D. & Klinman, J. P. Tunneling and dynamics in enzymatic hydride transfer. *Chem. Rev.* **106**, 3095–3118 (2006).
- Vendruscolo, M. & Dobson, C. M. Dynamic visions of enzymatic reactions. *Science* **313**, 1586–1587 (2006).
- Karplus, M. & McCammon, J. A. The internal dynamics of globular proteins. *Crit. Rev. Biochem.* **9**, 293–349 (1981).
- Kuriyan, J. & Weis, W. I. Rigid protein motion as a model for crystallographic temperature factors. *Proc. Natl Acad. Sci. USA* **88**, 2773–2777 (1991).
- Loria, J. P., Rance, M. & Palmer, A. G. A. TROSY CPMG sequence for characterizing chemical exchange in large proteins. *J. Biomol. NMR* **15**, 151–155 (1999).
- Mulder, F. A. A., Mittermaier, A., Hon, B., Dahlquist, F. W. & Kay, L. E. Studying excited states of proteins by NMR spectroscopy. *Nature Struct. Biol.* **8**, 932–935 (2001).
- Brooks, B. R. *et al.* CHARMM — a program for macromolecular energy, minimization, and dynamics calculations. *J. Comput. Chem.* **4**, 187–217 (1983).

Supplementary Information is linked to the online version of the paper at www.nature.com/nature.

Acknowledgements We thank V. Orekhov at the Swedish NMR Centre for 800 MHz NMR spectrometer time, L. Kay for providing pulse programs, D. Korzhnev for sharing software for NMR relaxation data analysis and J. Hohlbein for Monte Carlo simulation software. We are grateful to K. O. Stetter for providing DNA isolated from *A. aeolicus* and the Advanced Biomedical Computing Center for CPU hours. This work was supported by NIH grants to D.K. and K.A.H.-W., a DOE grant to D.K., a fellowship from the American Heart Association to M.L., a Volkswagen Foundation grant to C.G.H. and M.O., and the Studienstiftung des Deutschen Volkes to M.O. The research at Harvard was supported in part by a grant from NIH to M.K.

Author Contributions K.A.H.-W., V.T., M.L. and M.O. contributed equally to this work. V.T. solved the X-ray structures with assistance from T.F., E.P., M.A.W. and G.A.P. NMR experiments were performed by K.A.H.-W., V.T. and M.W.-W., with assistance from D.K. Computation was carried out by M.L., with assistance and supervision from M.K. and D.K. FRET experiments were designed and performed by M.O. and K.A.H.-W., with assistance and supervision from C.G.H. and D.K. K.A.H.-W. and D.K. wrote the manuscript, and D.K. supervised all aspects of this work.

Author Information The x-ray structures of *Aquifex* Adk and Zn•Ap5A-bound *Aquifex* Adk are deposited in the Protein Data Bank under ID code 2RH5 and 2RGX, respectively. Reprints and permissions information is available at www.nature.com/reprints. Correspondence and requests for materials should be addressed to D.K. (dkern@brandeis.edu) or C.G.H. (huebner@physik.uni-luebeck.de).

METHODS

Protein expression, purification and preparation. $^2\text{H}/^{15}\text{N}$ -labelled Adk with protonated amides was prepared by dialyzing purified protein against 6 M urea, pH 7, for 24 h followed by refolding in NMR buffer (40 mM MOPS, pH 7.0, and 50 mM NaCl). Fluorescently labelled Adk was prepared by reacting 100 μM aliquots of Y52C/V145C-6 \times His-tag mutants with 15-fold molar excess of Alexa633-maleimide and Alexa488-maleimide. Excess dye was removed using two consecutive PD-10 columns pre-equilibrated with FRET buffer (20 mM TRIS, pH 7.0, 50 mM NaCl). The final dye and protein concentrations were determined by absorbance and Lowry assay, respectively. Excess MTSL was removed from spin-labelled Adk using two consecutive PD-10 columns pre-equilibrated with NMR buffer to yield final samples of 0.7–1.0 mM protein in NMR buffer. The diamagnetic form of the spin label was prepared by adding threefold excess ascorbate from a 1 M stock in NMR buffer, and the sample pH was re-adjusted to 7.0.

X-ray crystallography structure determination. For crystallization, selenomethionine-labelled protein was expressed in B834 (DE3) methionine auxotrophe cell line (Novagen) as described (<http://alfi.mrc-lmb.cam.ac.uk/~ramak/madms/segrowth.html>), with the addition of 1 mM DTT to all buffers. Crystals of apo Adk were grown by the sitting-drop method using purified enzyme at 27 mg ml $^{-1}$ in 10 mM HEPES, pH 7.5. The drop contained a 1:1 mixture of protein solution and mother liquor (28–30% (w/v) PEG 3,000, 200 mM sodium acetate, and 100 mM TRIS, pH 8.5). Initial epitaxial twinned crystals were used for streak-seeding, yielding single and epitaxial twinned crystals. Crystals of Adk complexed with Zn^{2+} •Ap5A were obtained by the same method in the presence of 1 mM Ap5A and 50 mM MgCl_2 . The mother liquor was 25% (v/v) PEG MME 550, 0.1 M MES, pH 6.5, 0.01 M ZnSO_4 .

Diffraction data were collected at room temperature from a single capillary-mounted crystal at an in-house Rigaku 300B rotating anode X-ray generator and at the synchrotron beamline X6A at Brookhaven National Laboratory. A three-wavelength multiple anomalous dispersion (MAD) data set was collected on a single selenomethionine-labelled Adk crystal at 100 K. Unligated Adk crystals were cryo-protected using a 1:1 mixture of 70% (w/v) trehalose and were equilibrated with buffer. Co-complex crystals did not require any additional solutions for cryo-protection. Crystals were flash-cooled by immersion into liquid N_2 . Diffraction data were integrated and scaled with DENZO and SCALEPACK⁴⁹.

The co-complex structure of *Aquifex* Adk with Zn^{2+} •Ap5A was solved by molecular replacement using AMORE⁵⁰ in CCP4 (ref. 51) with 1AKE as the search model. A single copy of the molecule was located in the asymmetric unit (ASU). The model was manually rebuilt in O⁵² and refined with CNS⁵³. Model phases were used to calculate an anomalous difference map using FFT⁵⁴. Anomalous sites were modelled as zinc ions based on the presence of zinc sulphate in the mother liquor. This was confirmed from analysis of difference density maps. A final round of refinement was performed in REFMAC5 (ref. 55).

A combination of molecular replacement and MAD phasing techniques was required to determine the initial phases for the structure of ligand-free *Aquifex* Adk. Initial attempts at molecular replacement using AMORE and PHASER⁵⁶ with a number of adenylate kinase homologues located only a single copy in the asymmetric unit. A three-wavelength MAD data set was collected from a single crystal of selenomethionine-substituted Adk at wavelengths chosen to correspond to the peak, inflection point and high energy side of the selenium K edge as determined from an X-ray fluorescence scan of the Adk crystals (Supplementary Table 1). Determination of the location of the selenium sites using several methods yielded poor maps. The low quality of the maps is probably due to a low number of ordered selenomethionine sites in the asymmetric unit (6 methionines, excluding the 3 amino-terminal methionines, for 618 residues in the ASU), which resulted in phases of poor quality (0.68 and 0.53 figure of merit from SOLVE⁵⁷ and RESOLVE⁵⁸, respectively).

To improve the interpretability of the electron density maps and to ensure a consistent choice of origin, the initial molecular replacement solution was used to generate phases for the calculation of an anomalous difference Fourier map to locate nine selenium sites that were then used for MAD phasing. A new electron density map, calculated using combined molecular replacement and MAD phases, was interpretable and allowed us to locate the second molecule of Adk in the ASU. The phases calculated from the two-monomer model were combined with the MAD phases using sigmaA⁵⁹, and were improved using density modification in RESOLVE⁵⁸. An electron density map of satisfactory clarity was calculated with these density-modified phases and was used to guide manual rebuilding of the model in O. The model was refined with CNS and extended using automated structure building in ARP/wARP⁶⁰; electron density improvement was performed using the *Mycobacterium tuberculosis* (TB) structural genomics consortium bias removal server (<http://tuna.tamu.edu/>)⁶¹. After a number of rebuilding cycles, new fragments of density appeared outside of the

two-monomer model. ARP/wARP automatically built a poly-alanine model containing three α -helical fragments into this density.

Superposition of the complete monomer model over these fragments revealed a single docking possibility consistent with crystal packing. The third monomer was manually docked, rebuilt in O and refined with CNS. The final three-monomer model was refined to a final $R/R_{\text{free}} = 28/32$. Attempts to improve the R factors by refinement in the space group C222₁, and lower symmetry space groups C2, P2₁ and P1 did not affect R/R_{free} . The model was subsequently refined against the lower resolution, room temperature data. The final cycles of model building and refinement, including TLS refinement^{45,62}, were performed with Coot⁶³ and REFMAC5 (ref. 55). After TLS refinement, the final values of $R/R_{\text{free}} = 19.7/25.5$.

Three TLS models were tested and compared to the results of restrained refinement without inclusion of TLS parameters (Supplementary Table 2). The first TLS model treated all three molecules in the ASU as a single rigid group. The second treated each of the three monomers as separate rigid TLS groups. The third separated each molecule into the three standard nucleoside monophosphate domains: core (residues 1–29, 72–110 and 170–202), ATP lid (residues 111–169) and AMP lid (residues 30–71), giving a total of nine TLS groups for the ASU. TLS refinement was performed by first fixing the atomic B factors to 20 \AA^2 followed by ten cycles of TLS refinement and ten cycles of maximum likelihood restrained refinement of coordinates and B factors in REFMAC5. For all TLS models, all protein atoms were included for TLS refinement. Treatment of the ASU as a single TLS group (model 1) did not show any improvement over the isotropic B factor model (see Supplementary Table 2). However, both TLS models 2 and 3 led to improvements in both R and R_{free} when compared to the isotropic B-factor model. Model 3, which includes a TLS treatment for each domain of the three molecules in the ASU, provides the best fit to the data because it produces the lowest values for both R and R_{free} .

Crystal packing: conformational substates and B factors. The crystal environment of a protein is known to influence its conformation, particularly if the regions involved in crystal packing are flexible. Conformational heterogeneity of the mobile nucleotide-binding lids and less-ordered regions found within the three molecules in the ASU of apo Adk can be rationalized by considering the differences in crystal contacts for each molecule. Of the three molecules, molecule A has the most crystal contacts. Approximately 60% of the surface area of molecule A is buried in surface contact as compared to 39% and 40% of molecule B and molecule C, respectively (Supplementary Table 3 and Supplementary Figs 1 and 2). The significant amount of crystal contact and the uniform distribution of these contacts across molecule A probably limit its mobility and displacement within the ASU (Supplementary Fig. 1a), as judged by the quality of the electron density and by lower overall B factors and smaller TLS parameters (Supplementary Fig. 3 and Supplementary Table 2). In contrast, the core of molecule B has the poorest density as well as the highest overall B factors and largest TLS parameters compared to the core in the other two molecules (Supplementary Fig. 1b and Supplementary Table 2). This correlates well with the lack of crystal contacts in this region of molecule B (Supplementary Figs 1b and 2b). With the current data, we are unable to differentiate whether this disorder is caused by dynamic domain movement or static disorder of this region in the crystal.

Although molecules A and B have significant crystal contacts on the front and back side of their nucleotide-binding domains, where front and back refers to the surface of the domain facing towards or away from the nucleotide binding pocket, respectively, molecule C is missing contacts along the front side (Supplementary Figs 1c and 2c). The lack of crystal contact in the front regions of the nucleotide lids of molecule C and the presence of crystal contacts along the back of the lids are probably responsible for the observed partially closed conformation. The nucleotide lids of molecule A and molecule B are prevented from such compression by crystal-packing interactions with other symmetry copies (Supplementary Fig. 2a, b). The front side of molecule A interacts with a symmetry-related copy of itself and molecule B. These interactions limit the flexibility and displacement of the nucleotide lids. The ATP lid of molecule B, which is packed against the ATP lid and core of molecule A, is prevented from further displacement owing to the fact that the back of the ATP lid from molecule A is packed against the back of the AMP lid from molecule C. Having both domains pack into the interface between the nucleotide-binding lids of molecule B limits the movement of the nucleotide lids of molecule B. Molecule C, which is the most closed, only interacts with a portion of the AMP lid of molecule B. Because there are no interactions on the front side of the nucleotide lids, but there are packing interactions on the back side of the lid, the nucleotide lids are compressed towards the closed state.

In addition to the displacements leading to the three distinct substates in the crystal, different overall B factors are observed for molecule A, B and C. Whereas simulations of the three molecules in isolated water droplets show the largest

amplitude thermal fluctuations for the nucleotide lids with almost identical B factors for all three substrates (Supplementary Fig. 3), crystallographic B factors do not agree with these computational results. Overall B factors differ significantly in the three molecules (see text above and Supplementary Fig. 3), and can be rationalized well by the differences in crystal contacts described above. To test that protein rigid body displacement contributes to the observed high overall B factors, we extracted the TLS component and the residual component from the overall B factors using TLSANL⁶⁴ (Supplementary Fig. 3). The results clearly show that rigid body displacements with the domains defined above (TLS refinement) account for the differences in the overall B factors. After TLS refinement, the residual B factors (excluding the contribution of the refined TLS parameters) of all residues in all three molecules are between 40 and 60 (red line in Supplementary Fig. 3). **Relaxation dispersion NMR spectroscopy.** Spectra were acquired on 800, 600 and 500 MHz Varian NMR spectrometers. Backbone assignments at different temperatures and for the Mg²⁺•Ap5A-bound form were obtained by temperature titrations to transfer previously published backbone assignments¹³, and were confirmed by standard triple-resonance experiments. Relaxation data were fit to a two-site model describing the opening and closing of the nucleotide lids using the full Carver–Richards equation⁶⁵ with error analysis as described¹²:

$$R_2^{\text{eff}} = \frac{1}{2} \left(R_{2A}^0 + R_{2B}^0 + k_{\text{ex}} - \frac{1}{\tau_{\text{CP}}} \cosh^{-1} (D_+ \cosh \eta_+ - D_- \cosh \eta_-) \right) \quad (1)$$

$$\text{where } D_{\pm} = \frac{1}{2} \left(\frac{\psi + 2\Delta\omega_N^2}{\sqrt{\psi^2 + \zeta^2}} \pm 1 \right), \quad \eta_{\pm} = \frac{\tau_{\text{CP}}}{\sqrt{2}} \sqrt{\psi^2 + \zeta^2} \pm \psi,$$

$$\psi = (R_{2A}^0 - R_{2B}^0 - p_A k_{\text{ex}} + p_B k_{\text{ex}})^2 - \Delta\omega_N^2 + 4p_A p_B k_{\text{ex}}^2,$$

$$\zeta = 2\Delta\omega_N (R_{2A}^0 - R_{2B}^0 - p_A k_{\text{ex}} + p_B k_{\text{ex}}) \text{ and } v_{\text{CPMG}} = \frac{1}{2\tau_{\text{CP}}}. \text{ Here, } k_{\text{ex}} \text{ is the rate of}$$

exchange between states A and B, R_{2A}^0 and R_{2B}^0 are the inherent transverse relaxation rates in state A and B, respectively, and are assumed to be the same, p_A and p_B are the populations of state A and B, respectively, $\Delta\omega_N$ is the chemical shift difference between the two exchanging states, and τ_{CP} is the time between 180° pulses in the NMR experiment. We note that a two-state exchange is certainly an oversimplified model because both lids can move. However, the good correlation between $\Delta\omega$ calculated from the CPMG experiments and the $\Delta\omega$ measured for the open and closed conformations¹³ (Supplementary Table 4 and Supplementary Fig. 4) justifies such a simplification:

For Mg²⁺•Ap5A-bound Adk, $\Delta\omega_N$ values from the CPMG relaxation dispersion experiments ($\Delta\omega_N^{\text{CPMG}}$) were compared to the $\Delta\omega_N$ values between the open and closed state ($\Delta\omega_N^{\text{HSQC}}$) measured directly from the ¹⁵N–¹H heteronuclear single-quantum coherence (HSQC) spectra of apo (open) and Mg²⁺•Ap5A-saturated (closed) Adk samples (Supplementary Table 4). Although both Mg²⁺•Ap5A-saturated Adk and apo Adk sample open and closed conformations, as measured in the dispersion experiments, the HSQC spectra are indicative of the chemical shifts of the closed and open state, respectively, because the populations are highly skewed. For a number of residues spread throughout the protein but remote from the active site, very good agreement between $\Delta\omega_N^{\text{CPMG}}$ and $\Delta\omega_N^{\text{HSQC}}$ is observed. All of the residues with discrepancies between $\Delta\omega_N^{\text{CPMG}}$ and $\Delta\omega_N^{\text{HSQC}}$ can be explained by direct proximity to the inhibitor or proximity to additional metal-binding sites (Supplementary Fig. 4 and Supplementary Table 4). In the crystal structure of Adk bound to Zn²⁺•Ap5A, several Zn²⁺-binding sites are observed on the surface of the protein in addition to the Zn²⁺ in the active site. The side chains of residues that chelate the metal in these additional binding sites are shown in orange in Supplementary Fig. 4. The replacement of Mg²⁺ by Zn²⁺ in the crystal is due to the mother liquor. The NMR experiments are performed under saturating concentrations of Mg²⁺•Ap5A. The large NMR chemical shift differences between apo Adk and Mg²⁺•Ap5A-saturated Adk close to these Zn²⁺ sites is probably caused by Mg²⁺ binding to these locations.

Paramagnetic relaxation enhancement NMR. DTNB (5,5'-dithiobis(2-nitrobenzoic acid)) assays were performed⁶⁶ before and after labelling to confirm complete reaction of the Cys residue with the spin label. The HSQC spectra of the paramagnetic and diamagnetic forms of MTSL-*Aquifex* Adk(Y52C) were processed with only 5–10 Hz exponential broadening because a lorentzian line-shape is necessary for the single relaxation time analysis of paramagnetic relaxation effects⁶⁷. Distances were calculated from the intensity ratio of the HSQC spectra using R_2 values measured on the diamagnetic sample⁶⁸ and the following equations^{39,67,69}:

$$\frac{I_{\text{para}}}{I_{\text{dia}}} \approx \frac{R_2 \exp(-R_2^* t)}{R_2 + R_2^*} \quad (2)$$

$$d = \left[\frac{K}{R_2^*} \left(4\tau_c + \frac{3\tau_c}{1 + \omega_H^2 \tau_c^2} \right) \right]^{1/6} \quad (3)$$

where I_{para} and I_{dia} are the peak heights in the HSQC spectra of the paramagnetic and diamagnetic samples, respectively, R_2 is the amide proton R_2 measured on the diamagnetic sample, R_2^* is the additional relaxation due to the spin label, ω_H is the proton larmor frequency, K is the constant $1.23 \times 10^{-32} \text{ cm}^6 \text{ s}^{-2}$ for a nitroxide radical, and d is the distance between the proton and paramagnetic electron. τ_c is the electron–amide proton correlation time, which was assumed to be equal to the global tumbling time of the unlabelled protein²²—a good approximation in the case of a nitroxide spin label^{39,67}. The calculated distances from the PRE experiment on ligand-free Adk closely resemble the distances for the closed state except a few residues in the C-terminal helix have calculated distances a little shorter than in the closed state (Fig. 3e). This is probably due to the flexibility of the C-terminal helix as evidenced by R_{ex} for a number of residues in this helix (Fig. 3c).

NMR experiments on FRET-labelled samples. To compare directly the NMR and single-molecule FRET dynamics, several controls using the FRET-labelled samples for NMR experiments were performed. We note that the experiments described here do not provide an exact quantitative comparison owing to the technical difficulties addressed below; however, they do yield the accuracy needed for the conclusions drawn in the manuscript.

¹⁵N/¹H-*Aquifex* Adk(V145C/Y52C) with Alexa633 and Alexa488 attached at the cysteine residues was produced for NMR experiments on FRET-labelled Adk. First, ¹⁵N/¹H HSQC spectra were compared between the wild-type and FRET-labelled sample. Attachment of the bulky hydrophobic dyes resulted in severe line-broadening of all resonances, which was dependent on the protein concentration. This is indicative of transient intermolecular aggregation caused by the hydrophobic dyes. However, a decent NMR spectrum could be obtained at a protein concentration of 130 μM at 30 °C and 40 °C (Supplementary Fig. 5). Residues near the dye-attachment sites showed additional chemical shifts or extreme line broadening, as expected from the vicinity of the dyes and fluctuations of the bulky hydrophobic dyes resulting in intermediate timescale exchange. However, residues in the core of the protein could still be used to compare protein conformation between the wild-type and FRET-labelled Adk. Supplementary Fig. 5 shows that the chemical shifts of residues not near the fluorescent dyes are identical for wild-type and FRET-labelled apo Adk (blue and green spectra, respectively) and also for wild-type and FRET-labelled Mg²⁺•Ap5A-bound Adk (black and red spectra, respectively). This indicates that the distribution of mostly open conformations in apo Adk is not altered by attachment of the fluorescent dyes, and that the dyes do not affect Mg²⁺•Ap5A binding and lid closure.

Second, to compare quantitatively the single-molecule FRET kinetics (performed on protonated apo Adk at room temperature) with NMR kinetics, NMR dispersions were analysed on protonated apo Adk at 20 °C. ¹⁵N CPMG relaxation dispersion NMR experiments were performed initially on ¹⁵N/¹H apo Adk at 20 °C to compare the results with those previously obtained during turnover at 20 °C (ref. 13). However, the amplitude of exchange was small and the rate of exchange was fast (Supplementary Fig. 6a), preventing quantitative analysis of the data. Therefore, the experiments were repeated with ¹⁵N/²H apo Adk at 10 °C to increase the amplitude, decrease the rate and quantitatively determine the exchange parameters, as described in the main text. For a more quantitative comparison between the NMR and single-molecule FRET experiments, further analysis of the 20 °C protonated apo Adk relaxation dispersion profiles was performed to estimate the range of exchange rates compatible with the data. For this aim, residues with exchange in the ¹⁵N/¹H apo Adk 20 °C data set were fitted with fixed exchange rates between 2,000 s⁻¹ and 10,000 s⁻¹, and the R_2^0 values (R_2^{eff} at infinite v_{CPMG} with exchange fully suppressed) obtained from those fits were compared to the R_2^0 values of residues with no exchange (R_2^{eff} flat as a function of v_{CPMG}) (Supplementary Fig. 6b). As shown by the histogram of R_2^0 values across the protein, R_2^0 values fall between 15 s⁻¹ and 23 s⁻¹ (with a few exceptions). Comparison of this histogram with the distribution of fitted R_2^0 values for exchanging residues provides a means of estimating which exchange rates are most probable. Supplementary Fig. 6b shows that exchange rates between 2,000 s⁻¹ and 7,000 s⁻¹ are most consistent with the NMR data, in agreement with the single-molecule FRET experiments where the opening/closing rate at room temperature was measured as about 8,500 s⁻¹.

Third, the kinetics of lid motion was compared in wild-type and the FRET-labelled samples. The increased line-width of FRET-labelled Adk resulted in greater errors in the R_2 values, obscuring the small exchange contribution to the observed relaxation rate for apo Adk. Higher temperatures reduced the line-width but increased the rate out of the range accessible for CPMG experiments in the case of apo Adk. However, CPMG experiments could be performed on FRET-labelled Adk saturated with Mg²⁺•Ap5A at 30 °C (Supplementary Fig. 7). The exchange rate of wild-type Mg²⁺•Ap5A-bound Adk is about 300 s⁻¹ at 20 °C (see main text). At 30 °C, the exchange rate for Mg²⁺•Ap5A-bound FRET-labelled Adk is $600 \pm 300 \text{ s}^{-1}$ (mean \pm s.d.) (Supplementary Fig. 7). The error

is large, as expected because of slower tumbling, low protein concentration and fewer residues that can be monitored. The rate is faster than at 20 °C, as expected, and is comparable to the single-molecule FRET experiments performed at room temperature, which found an exchange rate of about 390 s⁻¹ for lid opening/closing.

Simulations. Molecule A, B and C of the apo *Aquifex* Adk crystal structure were simulated separately in water spheres with the stochastic boundary potential method^{70,71}, which prevents the solvent molecules from escaping from the spheres and provides a heat bath mimicking the surrounding solvent. The water molecules were represented as modified TIP3P⁷². The program Solvate 1.0 (by H. Grubmüller) was used to add a thick layer of water molecules and counter ions around the crystal structure of each molecule. Solvent molecules beyond 45 Å from the centre of each protein were deleted, leaving the minimum distance between the surfaces of water spheres and any protein atoms to be about 16 Å. The CHARMM 22-protein all-atom force field⁷³ was used in the simulations with the CMAP backbone energy correction included⁷⁴. Non-bonded interactions beyond 14 Å were shifted to be zero. The bond lengths between hydrogen and heavy atoms were fixed by the SHAKE algorithm⁷⁵. The time-step was 2 fs. To obtain the systems for starting the simulations, the protein and their surrounding solvent molecules were first minimized with gradually reducing harmonic constraints on protein backbone atoms. They were then slowly heated in 30 steps from 0 K to 300 K with 4 ps equilibration at each temperature step. The systems were then equilibrated at 300 K for 40 ps. The production runs were at 300 K for 10 ns. For the normal mode analysis³¹, the EEF1 implicit solvent model⁷⁶ was used. Quasi-harmonic (also called principal component) analysis³⁰ of the molecular dynamics trajectory was performed by diagonalizing the equal time mass weighted atom fluctuation cross-correlation matrix.

To investigate whether the ATP and AMP lids open and close in a correlated or independent fashion, we computed the normalized fluctuation correlation σ_{ij} between residual pairs as⁷⁷

$$\sigma_{ij} = \frac{\langle (\vec{r}_i - \langle \vec{r}_i \rangle) \bullet (\vec{r}_j - \langle \vec{r}_j \rangle) \rangle}{\sqrt{\langle (\vec{r}_i - \langle \vec{r}_i \rangle)^2 \rangle} \sqrt{\langle (\vec{r}_j - \langle \vec{r}_j \rangle)^2 \rangle}} \quad (4)$$

in which \vec{r}_i (\vec{r}_j) is the coordinate of the *i*th (*j*th) residue at a snapshot while the bracket indicates the average over all snapshots: σ_{ij} normalized to be between -1 and 1. When the motion between two residues is mostly anti-correlated (that is, when two residues are moving in opposite directions), σ_{ij} is negative and is coloured blue in Supplementary Fig. 8a. When the motion between two residues is mostly correlated (that is, when the two residues are moving in the same direction), σ_{ij} is positive and is coloured red in Supplementary Fig. 8a. When the motion of two residues is almost independent of each other, σ_{ij} is close to 0 and is coloured white in Supplementary Fig. 8a.

It is worth noting that σ_{ij} is influenced strongly by how the simulation trajectory is aligned onto the reference frame (Supplementary Fig. 8). When the simulation trajectory is aligned onto the crystal structure of the closed state by superimposing the whole protein, ATP and AMP lids seem to have anti-correlated motion, as indicated by the large blue block in the lower half-triangle of Supplementary Fig. 8a. In contrast, if only the core domain is superimposed during the alignment, the motion of the ATP lid is shown to be mostly independent of the motion of the AMP lid, as indicated by the large white block in the upper-half triangle of Supplementary Fig. 8a. Because our experimental NMR chemical shift data has shown that there are no internal conformational transitions in the core domain, the core domain serves as a better reference structure than the whole protein to study how the ATP and AMP lids fluctuate. Therefore, the core domain was used as a reference in the other analyses in this paper. Here, the correlation between the motion of the two lids is 0.12. The lack of correlation is further illustrated in a plot of the root mean square deviation fluctuations of the AMP and the ATP lid relative to the closed conformation (Supplementary Fig. 8b).

To investigate whether the simulation trajectories starting from molecule A, B and C of the apo crystal structure overlap with each other, we computed the backbone r.m.s. deviation between the closed state and snapshots of the simulations starting from the crystal structures of molecule A, B and C (Supplementary Fig. 9). Three conclusions can be drawn from the results. First, essentially the same conformational space is sampled in 10 ns molecular dynamics simulations starting from molecule A, B or C. Second, the fluctuations are centred around substate A. Third, the energy barriers between the crystallographically detected substates A, B and C are low because the transitions between them are easily sampled in nanosecond timescale simulations.

Single-molecule spectroscopy. Labelling sites in the lids were selected on the basis of distance changes between the open and closed conformations, considering only non-charged surface-exposed residues that faced away from the active site. Alexa488 and Alexa633 (Molecular Probes) were used as a FRET pair owing

to their high photostability and quantum yield and because of the well-suited Förster radius R_0 of approximately 48 Å. The reactivity of the cysteines was checked using DTNB⁶⁶ before labelling with the dyes. The labelling efficiency was between 98% and 100% as determined by a DTNB assay (which detects non-reacted Cys residues) and by absorbance. The protein concentration of the stock solution was determined by absorbance at 280 nm before labelling. After the reaction with the dyes, remaining free dye was removed by two PD-10 columns. No free dye could be detected after the second column. The concentration of the dyes attached to the protein was determined by absorbance, yielding 99–100% labelling efficiency. The ratio of the two dyes on the protein was 0.9:1.

The fluorescence quantum yields of the dyes bound to the protein were determined relative to the quantum efficiencies of the free dyes provided by the manufacturer. Single-site Cys mutants (Y52C, V145C) were made and reacted with either Alexa488 or Alexa633 to measure site-specific quantum yields. We determined quantum efficiencies for the donor Alexa488 of $Y_D^{ATP} = 0.77$ when attached to the ATP lid and of $Y_D^{AMP} = 0.74$ when attached to the AMP lid. For the acceptor Alexa633, those numbers are $Y_A^{ATP} = 0.53$ and $Y_A^{AMP} = 0.55$, respectively. The Förster radius R_0 was calculated according to the equation⁷⁸:

$$R_0 = (8.79 \times 10^{-5} n^{-4} Y_D J \kappa^2)^{1/6} (\text{Å}) \quad (5)$$

where n is the refractive index of the medium, Y_D is the donor fluorescence quantum yield, κ^2 is the orientation factor, and J is the overlap integral of donor emission and acceptor absorption. The latter was computed from the emission spectrum of the protein-bound donor and the absorption spectrum of the protein-bound acceptor, respectively. The site-dependent subtle changes of Y_D have negligible influence on R_0 owing to the inverse sixth power dependence. Time-resolved fluorescence polarization experiments yielded steady-state anisotropy values smaller than 0.1 for both dyes, irrespective of the labelling site. Therefore, the dyes are freely rotating, justifying $\kappa^2 = 2/3$ for the calculation of R_0 .

Samples with labelled molecules were diluted to a concentration of 100 pM in FRET buffer. Tween-20 (0.01% v/v, Carl Roth) helped to prevent surface adhesion of the molecules. For measurements of the molecules in presence of the inhibitor, 4 mM Ap5A and 2 mM MgCl₂ were added.

For the dye Alexa633, dark states on two different timescales—a 100 μs timescale and rare dark states lasting considerably longer (up to about 100 ms)—are observed in the experiments with immobilized protein (Fig. 5). We attribute the short dark states to triplet excursions and the longer ones to reversible photochemical reactions, probably a radical ionic state⁷⁹. Collective donor and acceptor dark states on the microsecond timescale are indicative of efficient singlet-triplet annihilation^{80,81}. This means that both dyes do not emit light if the acceptor is in the triplet state, essentially because this triplet state acts as an energy trap (see the section about time-resolved experiments).

Confocal optical microscope. Single-molecule measurements were performed with a home-built sample-scanning optical confocal microscope. Excitation light was provided by two lasers, a continuous wave external cavity diode laser operating at 488 nm (Protera, Novalux) and a pulsed diode laser delivering 100-ps pulses at 635 nm (LDH-P-635 + PDL 808 driver, Picoquant). Both lasers were fed into a single-mode fibre for spatial filtering. The light from the fibre was collimated by a ×4 microscope objective and reflected off a multichroic beam-splitter (z405/488/633, Chroma). Excitation light was eventually focused by a microscope objective (Nikon CFI Plan Apochromat 60 × 1.25 WI for diffusion measurements and CFI Plan Apochromat 100 × 1.4 oil for immobilized measurements) into the sample solution or onto the surface of a glass slide. A piezo-driven stage (P-734, Physik-Instrumente) operated in closed-loop allowed for positioning of the focal spot with nanometre precision.

Fluorescent light collected by the microscope objective passed several filters before being focused onto the detectors: the multichroic beam-splitter, a long-pass filter suppressing the 488 nm laser (HQ500LP, Chroma), and an additional bandpass filter (HQ532/70, Chroma) for the donor and a longpass filter (HQ650LP, Chroma) for the acceptor. Emission was split by a dichroic mirror (595DCXR, Chroma) into donor and acceptor components. The active area of the single-photon counting modules (SPCM AQ14, Perkin-Elmer) served as the confocal pinhole. The overall fluorescence-detection efficiency was 0.16 for the donor and 0.13 for the acceptor. Pulses from the detectors were fed into a TCSPC board (TimeHarp200, Picoquant) operating in the time-tagged time-resolved mode. The whole microscope was controlled by a programmable digital-signal processing unit (ADWin Gold, Jäger) and home-written software (LabView).

Shot-noise-limited performance of the setup^{82,83} was tested with a sample of fluorescent-energy-transfer latex spheres (TetraSpeck 0.1 μm, Molecular Probes) immersed in water. We chose this sample for its homogeneity and for the absence of transfer efficiency fluctuations. A FRET efficiency histogram of the reference sample along with a Monte Carlo simulation is shown

in Supplementary Fig. 11. The excitation intensity for this experiment was chosen in such a way that the detected fluorescence rate matched the rate in the Adk experiments. In the simulation, freely diffusing particles with poissonian emission in two channels with a distribution corresponding to the experiment were modelled. The almost perfect match of the experimental with the simulated histogram is clear evidence for shot-noise-limited performance of the microscope.

Single-molecule FRET diffusion measurements. For burst experiments, the donor was excited continuously at 488 nm with 40 μ W, whereas the acceptor was excited directly at 635 nm with 10 μ W by picosecond pulses at a repetition rate of 10 MHz. Detected photons were sorted by their arrival time (time resolution of about 35 ps) with respect to the pulsed laser trigger (10 MHz) for assignment to the respective excitation sources using a time window of 20 ns after the pulse, accounting for the mean lifetime of the acceptor of 3.1 ± 0.2 ns. Counted photons of each detector channel were binned at 1 ms and corrected for background counts, quantum yields of fluorescence of the dyes, and quantum efficiency of detection (including collection efficiency, filter transmission and detector efficiency). Fluorescence bursts were identified using two threshold criteria—one threshold for the integrated emission after donor excitation and one for emission on direct excitation of the acceptor—to select for molecules bearing both a donor and acceptor. Partial averaging owing to conformational transitions during transit through the focus was taken into consideration in the calculation of distances from E_i histograms. Because a direct calculation of absolute distances from FRET efficiencies is hampered by the difficulty of determining directly photon detection efficiencies in both detection channels and by the potentially biasing effect of dyes that are not freely rotating¹⁸, the Mg^{2+} •Ap5A-bound form was used as a reference point for the E_i value corresponding to the fully closed state.

Single-molecule FRET on immobilized samples. Glass slides were derivatized with *N*-(3-trimethoxysilyl)propyl)ethylene-diamine triacetic acid (Fluorochem) according to the manufacturer's procedure, and were chelated with Ni^{2+} (ref. 84). First, confocal images were taken at 100 nW continuous excitation at 488 nm to find molecules showing energy transfer, ensuring that both donor and acceptor were present. Individual molecules were then positioned in the focus and were excited continuously at 488 nm with a laser power of 2 μ W for Mg^{2+} •Ap5A-bound Adk and of 10 μ W and 30 μ W for ligand-free Adk.

The entire time traces of the two molecules shown in Supplementary Fig. 16a and Fig. 5d, but with an integration time of 10 ms shown in Supplementary Fig. 14a, b, correspondingly demonstrate the digital bleaching behaviour of the dyes characteristic of single-molecule observations. The temporal resolution is dictated essentially by the intensity of the signal. The laser intensity cannot be increased to arbitrary levels, because of the imminent photo-destruction. As seen in Fig. 5, the applied laser intensities enabled detection of individual events. Of a total of about 200 time traces for the ligand-free Adk and for Mg^{2+} •Ap5A-bound Adk, only 25 survived long enough for a statistical state analysis.

Changes between the open and closed states were identified on the basis of an extended threshold criterion. Instead of a single threshold value, a range of E_i values—a transition zone—was defined where the gaussian distributions of the open and closed states overlap in excess of 0.3. This overlap is caused by the shot noise of photon detection and by unresolved conformational substates. Within this range, an unambiguous assignment to either state is not possible. Therefore, E_i crossing of the transition zone indicates a change of state. The time instance where E_i is leaving the transition zone is identified as the change-of-state time. The lifetimes determined from the time traces were fitted exponentially excluding the first data point in the histograms because it contains shot-noise-induced apparent transitions.

To exclude artificial photo-induced effects on the apparent FRET dynamics, we performed control experiments at a threefold-increased laser intensity of 30 μ W. As Supplementary Fig. 15 shows, the rates at 10 μ W and 30 μ W laser intensity agree very well. For comparison, we performed a sample correlation analysis for immobilized apo Adk molecules. Here, an excitation intensity of 30 μ W delivered the least-noisy correlation.

The specificity of His-tagged Adk immobilization was tested in the following way. First, functionalized coverslips preincubated with imidazole did not show any binding (Supplementary Fig. 12a, b). Second, repeated washing of the coverslips with tethered Adk did not remove any molecules (Supplementary Fig. 12c, d). Third, washing with imidazole completely removed bound Adk (Supplementary Fig. 12e).

We performed a luciferase assay on the immobilized protein to ensure its functionality (Supplementary Fig. 13). A drop of buffer containing firefly luciferase, ADP and Mg^{2+} was deposited on top of a coverslip with immobilized labelled Adk.

For the assay, three different surface densities between 120–350 molecules per μm^2 were chosen. The surface density was determined from the total laser-induced fluorescence intensity of the tethered labelled Adk. For calibration, the

intensity of an image with a surface density low enough to allow for molecule counting was used (data not shown). The surface densities correspond to concentrations if the molecules were dissolved in the drop of buffer above the coverslip in the range of 0.1 nM to 0.3 nM. To test that all Adk molecules are tethered to the coverslip and are not released into solution, fluorescence correlation spectroscopy (FCS) was performed in the buffer solution above the coverslip. The FCS curve essentially resembled that of the buffer, meaning that only the same weakly fluorescent contaminants are present, and was clearly distinguishable from a 0.1 nM Adk solution measured as a reference.

Supplementary Fig. 13a shows the increase of luciferase chemoluminescence as a function of time for three different Adk surface densities. The assay performed under identical conditions on the coverslip with known ATP concentrations was used for calibration (Supplementary Fig. 13b). From the linear fits in Supplementary Fig. 13a, a turnover rate of $42 \pm 10 s^{-1}$ (mean \pm s.d.) per immobilized Adk molecule was obtained—a value very similar to the turnover rate for Adk measured with the coupled enzymatic assay. As the inset in Supplementary Fig. 13a demonstrates, there is a linear relationship between the Adk density and the slope of the chemoluminescence increase. This is proof for the quantitative validity of our surface-based assay.

Monte Carlo simulation of single-molecule time traces. To calculate the true opening and closing rates from the apparent rates, we generated simulated fluorescence intensity time traces (Supplementary Fig. 17). For the simulated time-traces, 10,000 exponentially distributed open and closed states including triplet dynamics were generated using Monte Carlo methods with a time resolution of 100 ns (identical to time resolution of photon counting). The data were then digitized in time bins according to the experimental conditions. Finally, the simulated time traces were analysed in exactly the same way as the experimental time traces. This procedure was iterated while changing the input parameters (lifetimes of open and closed states), until the analysis yielded the experimentally obtained apparent opening and closing rates (Supplementary Fig. 17a–d).

The simulations exemplify the following facts. First, they show clearly that the apparent rates extracted by a simple exponential fit of the experimental data (Supplementary Fig. 17a) yield slightly underestimated rates for ligand-free Adk owing to missed events (Supplementary Fig. 17c). Using simulations, the missed events can be predicted and then used to calculate the opening and closing rates. Our approach is similar to the missed event analysis for FRET data¹⁴ and for single-molecule ion channel recording⁸⁵, however, with triplet dynamics superimposed. Second, in contrast, for Mg^{2+} •Ap5A-bound Adk, the frequency of transitions is much slower than in ligand-free Adk (compare Supplementary Fig. 17a and 17b); this is specifically true for the opening rate, in agreement with our NMR data (Fig. 3a, b and Supplementary Fig. 6), resulting in a small overall number of transitions for a single time trace. This fact hampers an accurate states analysis. Moreover, the transition frequencies are now on the order of the occurrence of triplet dark states, significantly reducing the longer dwell times of the closed states (Supplementary Fig. 17b). Monte Carlo simulations further exemplify this fact, because the apparent opening rates ($110 s^{-1}$) are faster than the 'real' opening rates ($40 s^{-1}$, the input rates of the simulations) for Mg^{2+} •Ap5A-bound Adk. Third, the measured conformational transitions are clearly above the shot noise (Supplementary Fig. 17e, f), and our threshold analysis is robust for distinguishing between conformational transitions and shot-noise fluctuations (see Supplementary Fig. 17e, f). However, in the case of Mg^{2+} •Ap5A-bound Adk, shot noise does result in detectable reduction of the long dwell times of the closed state (Supplementary Fig. 17b, d, f). The acquisition of longer time traces for Mg^{2+} •Ap5A-bound Adk was not possible because of faster bleaching of the acceptor relative to ligand-free Adk owing to the higher energy transfer efficiency and consequently preferred excitation of the acceptor. Fourth, simulated and experimental time traces look similar in respect to 'noisiness', supporting the fact that the observed fluctuations in E_i within states are mainly caused by shot noise. Fifth, the E_i histograms of the simulated traces resemble those of the experimental traces quite nicely, whereas the corresponding histograms of pure shot noise are clearly distinct. There is some additional width in the histograms from the experiment, suggesting the possibility that there are more than just two states.

Correlation analysis of single-molecule time traces. Auto- and cross-correlation functions calculated for individual apo Adk molecules, and subsequently averaged, are shown in Fig. 5g. A global fit was performed with a model similar to that used in ref. 38 with included singlet–triplet annihilation:

For the acceptor and donor autocorrelation:

$$AC(t) = 1 - f(t) + A + B / ((1 - C)(1 - T))(1 - C + Ce^{-kt})(1 - T + Te^{-t/\tau_2 T}) \quad (6)$$

and for the cross-correlation:

$$CC(t) = 1 - f(t) + A + B(1 + Ce^{-kt})(1 + Te^{-t/\tau_1}) \quad (7)$$

were used as fitting functions, where A and B are constants, T is the triplet

fraction, τ_T is the triplet decay, and C is the additional correlated or anticorrelated fraction with k , the overall FRET dynamics rate constant. τ_T was determined by FCS of diffusing molecules and set to be 3.5 μ s, whereas the rate constant k was fit simultaneously. The function $f(t)$ was used to describe the drop of the correlation function owing to the cutoff effect.

In the donor–acceptor cross-correlation function, an anti-correlation is prominent for the times between 10^{-4} s and 10^{-3} s. Both autocorrelation functions, that of the donor and that of the acceptor, show a correlation with the same time constant. This finding of an anti-correlation in the cross-correlation function with corresponding decays in the correlation functions of the donor and the acceptor provides clear evidence for E_i fluctuations. The overall rate of these fluctuations is $7,000 \pm 1,500 \text{ s}^{-1}$ (mean \pm s.d.), in very good agreement with the overall rate of $8,500 \pm 700 \text{ s}^{-1}$ (mean \pm s.d.) obtained from state analysis. This rate also matches quite well the total rate obtained from NMR.

At shorter times (few microseconds), a correlation is present in all correlation functions, in the cross-correlation as well as in the auto-correlation functions. We assign this correlation time of 3.5 μ s to triplet excursions of the donor and the acceptor, respectively, apparently leading to correlated intensity fluctuations of both dyes. This correlation again strongly indicates efficient singlet–triplet annihilation. Overall triplet correlation times for the Adk-bound donor of $3.9 \pm 0.2 \mu$ s (mean \pm s.d.) and for the Adk-bound acceptor of $3.8 \pm 0.2 \mu$ s (mean \pm s.d.) were independently determined in solution for excitation rates comparable to those in the time-resolved FRET experiments (data not shown).

For inhibitor-bound Adk, we find similar behaviour (Supplementary Fig. 16d). However, the amplitude of the anti-correlated term in the cross-correlation function is extremely small because of the large ratio between the opening/closing rates expected from NMR dynamics. Therefore, a fit of the experimental data, such as for Apo Adk, yields very large errors. We can only give the order of magnitude of the overall rate of these fluctuations, which is $1,000 \text{ s}^{-1}$, in reasonable agreement with the state analysis and with the kinetics from NMR spectroscopy.

Single-label control experiments. An independent control experiment was performed on singly donor- or acceptor-labelled Adk to rule out that acceptor or donor dye fluctuations and not true energy transfers are causing the observed transfer efficiency fluctuations. The result supports our finding from the states analysis and the cross-correlation analysis because the donor- and acceptor-only time traces are shot-noise-limited with superimposed triplet dark states (Supplementary Fig. 18).

On request, we can provide all original time traces for those who want to perform their own types of analysis.

49. Otwinowski, Z. & Minor, W. Processing of X-ray diffraction data collected in oscillating mode. *Methods Enzymol.* **276**, 307–326 (1997).
50. Navaza, J. AMORE — an automated package for molecular replacement. *Acta Crystallogr. A* **50**, 157–163 (1994).
51. Collaborative Computational Project, Number 4. The CCP4 Suite — programs for protein crystallography. *Acta Crystallogr. D* **50**, 760–763 (1994).
52. Jones, T. A., Zou, J. Y., Cowan, S. W. & Kjeldgaard, M. Improved methods for building protein models in electron-density maps and the location of errors in these models. *Acta Crystallogr. A* **47**, 110–119 (1991).
53. Brunger, A. T. *et al.* Crystallography & NMR system: a new software suite for macromolecular structure determination. *Acta Crystallogr. D* **54**, 905–921 (1998).
54. Immirzi, A. in *Crystallographic Computing Techniques* (ed. Ahmed, F. R.) 399–412 (Munksgaard, Copenhagen, 1976).
55. Murshudov, G. N., Vagin, A. A. & Dodson, E. J. Refinement of macromolecular structures by the maximum-likelihood method. *Acta Crystallogr. D* **53**, 240–255 (1997).
56. Read, R. J. Pushing the boundaries of molecular replacement with maximum likelihood. *Acta Crystallogr. D* **57**, 1373–1382 (2001).
57. Terwilliger, T. C. & Berendzen, J. Automated MAD and MIR structure solution. *Acta Crystallogr. D* **55**, 849–861 (1999).
58. Terwilliger, T. C. Maximum-likelihood density modification. *Acta Crystallogr. D* **56**, 965–972 (2000).
59. Read, R. J. Improved Fourier coefficients for maps using phases from partial structures with errors. *Acta Crystallogr. A* **42**, 140–149 (1986).
60. Perrakis, A., Morris, R. & Lamzin, V. S. Automated protein model building combined with iterative structure refinement. *Nature Struct. Biol.* **6**, 458–463 (1999).
61. Reddy, V. *et al.* Effective electron-density map improvement and structure validation on a Linux multi-CPU web cluster: the TB structural genomics consortium bias removal Web service. *Acta Crystallogr. D* **59**, 2200–2210 (2003).
62. Schomaker, V. & Trueblood, K. N. On rigid-body motion of molecules in crystals. *Acta Crystallogr. B* **24**, 63–76 (1968).
63. Emsley, P. & Cowtan, K. Coot: model-building tools for molecular graphics. *Acta Crystallogr. D* **60**, 2126–2132 (2004).
64. Howlin, B. & Butler, S. A. Moss, D. S., Harris, G. W. & Driessen, H. P. C. TLSANL — TLS parameter-analysis program for segmented anisotropic refinement of macromolecular structures. *J. Appl. Cryst.* **26**, 622–624 (1993).
65. Carver, J. P. & Richards, R. E. A general two-site solution for the chemical exchange produced dependence of T2 upon the Carr–Purcell pulse separation. *J. Magn. Reson.* **6**, 89–105 (1972).
66. Riddles, P. W., Blakeley, R. L. & Zerner, B. Ellman's reagent: 5,5'-dithiobis(2-nitrobenzoic acid) — a reexamination. *Anal. Biochem.* **94**, 75–81 (1979).
67. Battiste, J. L. & Wagner, G. Utilization of site-directed spin labeling and high-resolution heteronuclear nuclear magnetic resonance for global fold determination of large proteins with limited nuclear overhauser effect data. *Biochemistry* **39**, 5355–5365 (2000).
68. Donaldson, L. W. *et al.* Structural characterization of proteins with an attached ATCUN motif by paramagnetic relaxation enhancement NMR spectroscopy. *J. Am. Chem. Soc.* **123**, 9843–9847 (2001).
69. Solomon, I. & Bloembergen, N. Nuclear magnetic interactions in the HF molecule. *J. Chem. Phys.* **25**, 261–266 (1956).
70. Brooks, C. L. & Karplus, M. Deformable stochastic boundaries in molecular-dynamics. *J. Chem. Phys.* **79**, 6312–6325 (1983).
71. Brunger, A., Brooks, C. L. & Karplus, M. Stochastic boundary-conditions for molecular-dynamics simulations of ST2 water. *Chem. Phys. Lett.* **105**, 495–500 (1984).
72. Price, D. J. & Brooks, C. L. A modified TIP3P water potential for simulation with Ewald summation. *J. Chem. Phys.* **121**, 10096–10103 (2004).
73. MacKerell, A. D. *et al.* All-atom empirical potential for molecular modeling and dynamics studies of proteins. *J. Phys. Chem. B* **102**, 3586–3616 (1998).
74. MacKerell, A. D., Feig, M. & Brooks, C. L. Extending the treatment of backbone energetics in protein force fields: limitations of gas-phase quantum mechanics in reproducing protein conformational distributions in molecular dynamics simulations. *J. Comput. Chem.* **25**, 1400–1415 (2004).
75. Ryckaert, J. P., Ciccotti, G. & Berendsen, H. J. C. Numerical-integration of cartesian equations of motion of a system with constraints — molecular-dynamics of N-alkanes. *J. Comput. Phys.* **23**, 327–341 (1977).
76. Lazaridis, T. & Karplus, M. Effective energy function for proteins in solution. *Proteins* **35**, 133–152 (1999).
77. Ichiye, T. & Karplus, M. Collective motions in proteins — a covariance analysis of atomic fluctuations in molecular-dynamics and normal mode simulations. *Proteins* **11**, 205–217 (1991).
78. Lakowicz, J. R. *Principles of Fluorescence Spectroscopy* page 446 (Springer, New York, 2006).
79. Zondervan, R., Kulzer, F., Orłinskii, S. B. & Orrit, M. Photoblinking of rhodamine 6G in poly(vinyl alcohol): radical dark state formed through the triplet. *J. Phys. Chem. A* **107**, 6770–6776 (2003).
80. Vosch, T. *et al.* Probing Förster type energy pathways in a first generation rigid dendrimer bearing two perylene imide chromophores. *J. Phys. Chem. A* **107**, 6920–6931 (2003).
81. Hübner, C. G. *et al.* Photon antibunching and collective effects in the fluorescence of single bichromophoric molecules. *Phys. Rev. Lett.* **91**, 093903 (2003).
82. Antonik, M., Felekyan, S., Gaiduk, A. & Seidel, C. A. M. Separating structural heterogeneities from stochastic variations in fluorescence resonance energy transfer distributions via photon distribution analysis. *J. Phys. Chem. B* **110**, 6970–6978 (2006).
83. Nir, E. *et al.* Shot-noise limited single-molecule FRET histograms: comparison between theory and experiments. *J. Phys. Chem. B* **110**, 22103–22124 (2006).
84. Kaim, G. *et al.* Coupled rotation within single F₀F₁ enzyme complexes during ATP synthesis or hydrolysis. *FEBS Lett.* **525**, 156–163 (2002).
85. Blatz, A. L. & Magleby, K. L. Correcting single channel data for missed events. *Biophys. J.* **49**, 967–980 (1986).